Available online at www.sciencedirect.com
ScienceDirect
Journal of Computational Physics 226 (2007) 1808–1829
JOURNAL OF COMPUTATIONAL PHYSICS
www.elsevier.com/locate/jcp

Modeling the interaction of biological cells with a solidifying interface ☆

Anthony Chang [a,*], Jonathan A. Dantzig [a], Brian T. Darr [b], Allison Hubel [b]

[a] Department of Mechanical Science and Engineering, University of Illinois at Urbana-Champaign, 1206 W. Green Street, Urbana, IL 61801, USA
[b] Department of Mechanical Engineering, University of Minnesota, 111 Church Street SE, Minneapolis, MN 55255, USA

Received 15 December 2006; received in revised form 23 May 2007; accepted 30 May 2007
Available online 29 June 2007

Abstract

In this article, we develop a modified level set method for modeling the interaction of particles with a solidifying interface. The dynamic computation of the van der Waals and drag forces between the particles and the solidification front leads to a problem of multiple length scales, which we resolve using adaptive grid techniques. We present a variety of example problems to demonstrate the accuracy and utility of the method. We also use the model to interpret experimental results obtained using directional solidification in a cryomicroscope.

Keywords: Particle pushing; Level set methods; Solidification; Cryopreservation; Cell dehydration

1. Introduction

Cryopreservation is an important method for preserving cells, tissues and other biological materials. In a typical freezing procedure the cells are suspended in a specialized solution and then cooled at a controlled rate. The nucleation of ice crystals in the extracellular solution at temperatures between −5 and −15 °C leads to significant changes in the local environment surrounding the cells. The rejection of solute by the solidification front exposes cells to high concentrations close to the interface. Cells frozen at a slow rate will be exposed to these high concentration regions ahead of the interface for an extended period of time, which leads to a decrease in post-thaw viability [20,23,35,36,38,39]. Cells can also become trapped in the solidifying medium, which can induce mechanical deformation of the cellular membrane. Cells are capable of resisting mechanical damage to a certain extent, but the stress induced by the solidification front may lead to cell membrane

☆ This work was supported in part by the National Aeronautics and Space Administration (NNC04GA46G) and the National Science Foundation (DMR-01-21695).
* Corresponding author. Tel.: +1 217 979 9979.
E-mail addresses: a-chang3@hotmail.com (A. Chang), dantzig@uiuc.edu (J.A. Dantzig), darrx001@umn.edu (B.T. Darr), hubel001@umn.edu (A. Hubel).

0021-9991/$ - see front matter
doi:10.1016/j.jcp.2007.05.039

rupture [23,24]. The cell responds to these changing environmental conditions by expressing water or forming intracellular ice crystals. The onset of intracellular ice formation is almost always lethal [10,33,37]. The complex interaction between damage mechanisms leads to an interesting optimization problem where slow freezing exposes the cells to lethal concentrations of electrolytes, while rapid cooling increases the probability of intracellular ice formation. The objective of this work is to develop models of the interaction of cells with a solidifying interface, in order to better understand this complex problem.

Relatively little work has been done to characterize either theoretically and experimentally the motion of cells with respect to the interface for different solidification microstructures and the effects that this might have on cell survival rates. Cells can be engulfed into the advancing interface, pushed into interdendritic regions or sequestered by secondary branches. One computational study simulated the interactions between the advancing interface and cells, using very high cooling rates (100–10,000 °C/min) [31]. These simulations predicted water content of the cell as a function of temperature for different solidification morphologies. Another computational study examined the effects of cell volume change on the morphology of the interface during engulfment [5]. Motion of the cells with respect to the interface (partitioning) was not included in either of these models. This partitioning can influence the chemical and mechanical history experienced by the cell.

Cryoprotectants are frequently added to the solution in order to reduce damage to the preserved cells. Numerous mechanisms have been proposed for the cryoprotection imparted to the cells, including osmotic expression of water from the cells into the solute-rich medium, stabilization of the cell membrane by the cryoprotectant [50,55], and suppression of ice crystallization in the medium and/or within the cells [8]. The addition of cryoprotectants can also affect the morphology of the interface [20] and the surface energy between the cell and the ice interface [53]. Our work will show that different cell/interface interactions can produce different local environments around the cell that may be beneficial in protecting the cell from damage.

In order to study the interaction between cells and a solidification front, we have performed both experimental studies and numerical simulations. This article focuses on the numerical methods, and therefore, we give only a brief description of the experiments and a gallery of results to illustrate the phenomena we wish to capture in the modeling effort. The experiments were performed using a specially-developed directional solidification apparatus, capable of controlling the temperature gradient and interface velocity independently, at appropriate cryogenic temperatures. Lymphoblasts, spherical cells approximately 15 μm in diameter, were suspended in both isotonic saline solution and in saline solution augmented by various concentrations of trehalose.

At low velocity, the liquid–solid interface remains flat. If the velocities are sufficiently low, the cells are simply pushed ahead of the interface leading to a pileup of cells at the solidification front, as illustrated in the sequence of micrographs shown in Fig. 1a. At higher velocity (see Fig. 1(b)), the cells begin to affect the interface morphology, creating ''pockets'' which eventually engulf the cell. The mechanism for this behavior is that the cells interfere with the local solute transport ahead of the interface, thus limiting the ability of the interface to grow. Once the cell is engulfed, the interface ''heals'' and catches up to the rest of the interface, which is still in the morphologically stable regime.

As the solidification velocity increases further, the interface becomes morphologically unstable, and shallow grooves begin to appear. These morphological features are usually called cells, which has the potential to be confusing in the current context. Accordingly, we will refer to this pattern as ''grooves''. A sequence taken from this regime is shown in Fig. 2. Several new phenomena appear: cells can be entrapped by a pre-existing groove (Feature A); cells may be displaced laterally along the interface until they are captured by a groove (Feature B); and cells can be engulfed by a groove of their own making in the interface that then persists after their incorporation (Feature C). Notice also that the cells become darker and slightly smaller as they approach the interface, indicative of water expression from the cells into the surrounding solute-rich liquid. Measurements of the cell volume as a function of its position will allow us to infer from the experiments the physical parameters associated with expression of water from the cell.

At still higher velocities, the interface becomes dendritic. The phenomena already identified, i.e., lateral translation of cells, tip splitting and capture in the morphological interstices are all present in this case as well. An example is shown in Fig. 3.

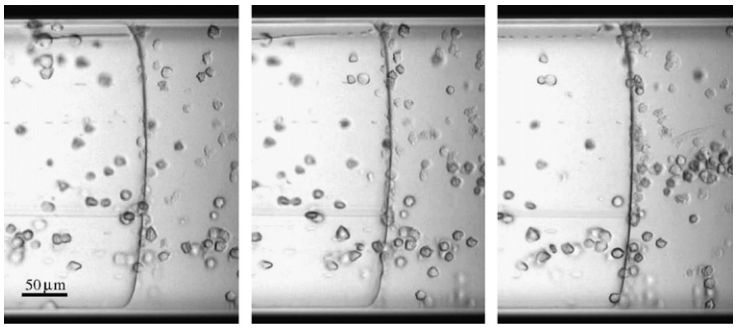

(a) $V = 1\mu\mathrm{m/s}$, cells pushed ahead of the interface

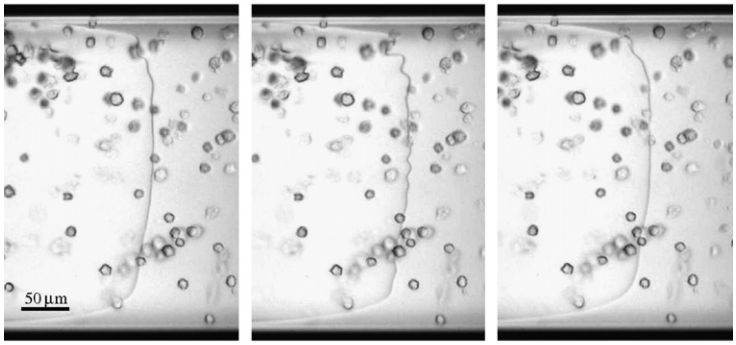

(b) $V = 4\mu\mathrm{m/s}$, cells engulfed by interface.

Fig. 1. Cells interacting with a morphologically stable (flat) ice interface. The applied thermal gradient is 1.933×10^4 K/m, and the width of the field in each micrograph is approximately 100 μm.

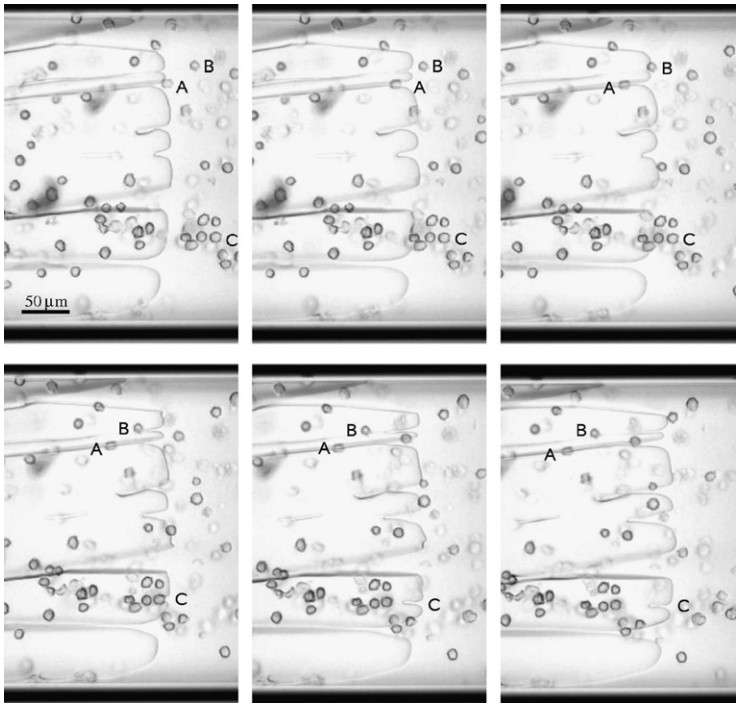

Fig. 2. Cell capture by an interface at $V = 5$ μm/s, just over the morphological stability limit. Notice that cells may be captured by existing grooves in the interface (A), they may translate to an existing groove (B), and the engulfment of cells can lead to persistent depressions in the interface (C).

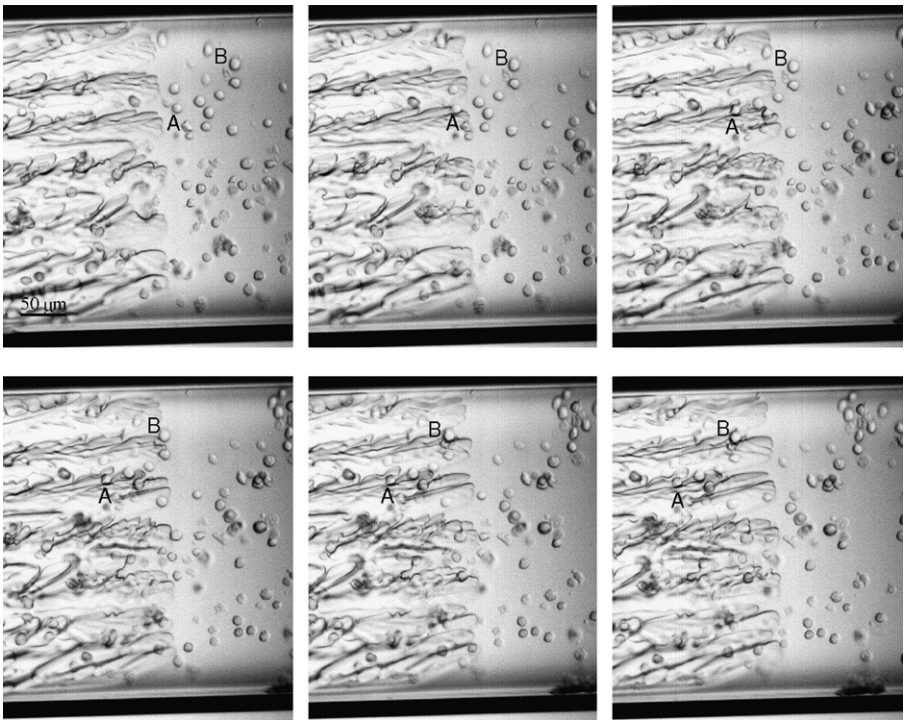

Fig. 3. Cell capture by an interface at $V = 20$ μm/s. Notice that particle interaction can lead to tip splitting (A) or tip termination (B).

This gallery of results motivates the computational work that is the main focus of this paper. We will develop a numerical model for the cryopreservation process capable of capturing the important features and phenomena seen in the experiments. These include: complex interface morphologies corresponding to the planar, cellular and dendritic growth regimes; interaction of these complex interfaces with cells suspended in the liquid, including pushing, capture and engulfment; and a detailed representation of the solute field in the liquid and its effect on the cells. This will allow us to augment the experimental observations with data that are very difficult to obtain experimentally, in order to interpret the results. With this motivation, we now describe some of the relevant prior work modeling solidification morphologies and interaction of inert particles with such interfaces.

The evolution of solidification microstructure in alloys has been studied extensively. The principal difficulty is the tracking of the liquid–solid interface as it evolves as part of the solution of the temperature and solute fields. In the so-called sharp interface model, boundary conditions for the temperature and solute are specified on the interface, corresponding to conservation of energy, conservation of solute, and the assertion of thermodynamic equilibrium at the interface. It can be difficult to ensure that the grid conforms to the interface as it evolves, making it difficult to solve the sharp interface problem directly. Two well-developed techniques for solving the problem using a fixed grid, while satisfying the interface conditions implicitly, are the phase-field method and the level set method.

The phase-field method introduces an order parameter $\phi \in [-1, 1]$ such that $\phi = 1$ corresponds to the solid, $\phi = -1$ corresponds to the liquid, and intermediate values correspond to the interface. The formulation ensures that the diffuse interface remains thin [11,16,25,26,41,45]. Proper selection of the constants in the phase-field free energy ensures that the phase-field model converges to the sharp interface model when operated in the appropriate limits [26]. In problems such as the one we are interested in here, one must use some sort of adaptive grid in order to resolve the multiple length scales corresponding to the interface width and the external diffusion fields [2,25].

The level set method has also been used successfully to model dendritic growth in pure materials [7,15,27]. This method locates the interface implicitly on an underlying fixed grid, and satisfies the boundary conditions

in two steps: the temperature and/or solute field is computed using the condition of thermodynamic equilibrium on the (unmoving) interface, and then the interface position is evolved using the energy and/or solute balance boundary condition. The interface motion is achieved by solving a pure advection equation for a signed distance function that indicates the distance from the interface. The level set method offers certain advantages for the problem at hand. The forces between the cells and the moving interface depend on the distance of separation between them, a quantity that arises naturally in the level set formulation. We are also interested in binary alloy systems that may not have a convenient free energy representation. For these reasons, we chose to implement our model using the level set method.

In addition to modeling the development of the interface morphology, we must also represent its interaction with cells suspended in the liquid. The basic model for the interaction of a particle with a flat solidifying interface was developed by Pötschke and Rogge [43], who described the interaction as a competition between repulsive van der Waals forces, and drag forces on the moving particle that oppose its motion away from the interface. The van der Waals force depends on the distance between the particle and interface, while the drag force depends on the velocity. There is thus a critical interface velocity below which cells are pushed ahead of the interface and above which they are engulfed. Several authors have extended the basic model of Pötschke and Rogge to other forces. For example, Stefanescu et al. added buoyant forces, and were able to obtain good agreement between their analytical calculations and experimental observations [46,49]. A linear stability analysis has also shown that the presence of the particles themselves may affect the morphological evolution of the interface [17].

Numerical methods have also been used to model the interaction of particles. These studies include, for example, the effect of different thermal conductivity of the particle and the medium [46]. Most of these studies consider a fixed configuration of the particle and the interface. Some dynamic simulations of the drag force induced by the pushing of a particle by an advancing interface have also been done [6,13,14]. These numerical models, like the analytical models of the preceding paragraph, are limited to describing the forces between a particle and a single interface that is flat or slightly curved, and often describe only steady state behavior between the particle and the interface. They also generally apply axisymmetry as a boundary condition to simplify the calculation of the van der Waals forces. Most of these types of simulations were performed for pure materials, which is not appropriate for cryopreservation. Thus, none of the previous results are sufficient to study the complex interface interactions that we expect to encounter. In the next section, we will describe a method for incorporating the calculation of the interaction forces directly into the numerical calculations for the interface evolution. These forces are calculated without assuming a specific geometry for the problem and are more accurate for our purposes. We will also discuss a method for simulating the solidification of alloyed materials such as those found in cryopreservation.

This article is organized as follows. In the next section, we describe the numerical methods used for modeling interface evolution, computing the forces acting between the cells and the advancing interface, and an adaptive grid scheme implemented for computational efficiency. We then present several test problems to verify the accuracy of the various parts of the model. Finally, we present a series of simulations that examine the interaction of cells with solidification fronts of various morphologies, and where possible make comparisons to experimental results.

2. Numerical procedures

2.1. Level set method

We discuss the numerical methods used in the context of the model of the directional solidification experiments described in Section 1. In this apparatus, a suspension of cells is sealed in a rectangular capillary that is then placed on two blocks held at fixed temperature and separated by a fixed distance. This sets the temperature gradient for the experiment. The capillary tube is then pulled at a constant velocity, V_0, across the fixed temperature blocks. The thermal diffusivities of the suspension and capillary are much greater than the chemical diffusivity in the liquid or solid, and we therefore invoke the so-called ''frozen temperature approximation'', where the temperature field is assumed to be unaffected by the solidification process, and the

temperature gradient is assumed to be constant. The problem then reduces to solving for the concentrations in the solid and liquid phases.

The governing equations for the solute are

$$\frac{\partial C_s}{\partial t} + \mathbf{v} \cdot \nabla C_s = D_s \nabla^2 C_s \quad \text{solid}, \tag{1}$$

$$\frac{\partial C_\ell}{\partial t} + \mathbf{v} \cdot \nabla C_\ell = D_\ell \nabla^2 C_\ell \quad \text{liquid}, \tag{2}$$

where $C_{s,\ell}$ are the concentrations in the solid and liquid, respectively, $\mathbf{v}_{s,\ell}$ are the velocities, and $D_{s,\ell}$ are the corresponding chemical diffusivities, each assumed to be constant. In the simulations, we will solve these equations in a frame translating with the pulling velocity of the apparatus, V_0. The simulations will all be performed in a rectangular domain with temperature increasing from left to right, and periodic boundary conditions on the top and bottom.

Solute balance is enforced at the interface, in the form

$$D_s \nabla C_s \cdot \mathbf{n} - D_\ell \nabla C_\ell \cdot \mathbf{n} = \mathbf{V}^i \cdot \mathbf{n}(D_\ell C_\ell^i - D_s C_s^i) = V_n(D_\ell C_\ell^i - D_s C_s^i), \tag{3}$$

where the superscript i refers to values at the interface, $\mathbf{V}^i$ is the interface velocity and $\mathbf{n}$ is the local normal to the interface. We have also introduced the shorthand notation V_n for the normal component of the interface velocity. Note that in general V_n is not equal to V_0. The final condition that we enforce is that the interface is in thermodynamic equilibrium. The compositions of the solid and liquid are therefore given by the equilibrium phase diagram, whose liquidus and solidus curves are written in functional form as $T_{liq}(C_\ell)$ and $T_{sol}(C_s)$, respectively. Most numerical simulations of directional solidification in the literature have used an idealized version of the phase diagram [11,45] where the liquidus and solidus curves are linearized. In our formulation, the concentration fields in the solid and the liquid phases are solved separately, coupled only by a boundary condition on the flux. There is no particular advantage to linearizing the phase diagram, and so we represent the solidus and liquidus curves using a lookup table that associates the interface temperature with a specific jump in the concentration. Recall that the interface temperature is already known because we use the frozen temperature approximation, and the concentration can be calculated using the phase diagram information. The ability to specify an arbitrary phase diagram is very convenient for the problem at hand.

The statement of thermodynamic equilibrium is then

$$T^i = T_{liq}(C_\ell^i) - \Gamma\kappa = T_{sol}(C_s^i) - \Gamma\kappa, \tag{4}$$

where Γ is the Gibbs–Thomson coefficient (the ratio of the surface energy γ to the entropy of fusion) and κ is twice the mean curvature. We note that Eq. (4) is written assuming that interface kinetics are negligible. All of our simulations are performed in 2D, where anisotropy of the surface energy can be included by writing $\Gamma = \Gamma_0 + \Gamma_{\theta\theta}$, where θ is the angle of the normal vector with respect to a basis vector. For example, for fourfold symmetry we have $\Gamma = \Gamma_0(1 - 15\epsilon_4 \cos 4\theta)$. The parameter ϵ_4 represents the strength of the anisotropy. The far-field concentration boundary condition is set to the nominal composition of the alloy C_0, and the boundaries parallel to the pulling velocity are taken as periodic.

The solidification problem is solved using the level set method developed by Gibou et al. [15] The reader is referred to that paper for the details of the method, and we discuss here only those aspects that are either important to understand the results, or which are specialized to our implementation. In the level set method, a signed distance function, ϕ, is introduced whose value corresponds to the normal distance of any point to the advancing interface, and whose sign indicates whether the location is in the solid (negative) or liquid (positive). The interface is identified as the level set $\phi = 0$. The algorithm proceeds in four basic steps, each of which is explained further below:

(1) Given a known concentration field and location of the interface (which may be the initial condition), compute the normal velocity of the interface V_n using Eq. (3).
(2) Relocate the interface by advecting the distance function using V_n.
(3) Reinitialize ϕ so that it once more represents a distance function.
(4) Solve for the concentration fields in the solid and liquid, using Eq. (4) as a boundary condition.

The extraction of V_n from Eq. (3) in the first step is straightforward. Once V_n is known, the interface is advanced by solving a pure advection equation for the distance function, ϕ:

$$\frac{\partial \phi}{\partial t} + V_n |\nabla \phi| = 0. \tag{5}$$

One must be careful in the numerical solution of Eq. (5), because errors in its solution can lead to mass loss, instability, and/or spurious oscillations in the interface position. To minimize these problems, a fifth-order WENO (weighted essentially non-oscillatory) method is used to discretize space and a third-order Runge–Kutta method is used to discretize time. The overall accuracy of the algorithm is first order, resulting from the discrete form used to evaluate the concentration gradient in the calculation of the interface velocity. The new value of ϕ is no longer a distance function after the advection step. The reinitialization process, described by Fedkiw et al. [12], is used to return ϕ to its interpretation as a distance function by solving:

$$\frac{\partial \phi}{\partial \tau} + S(\phi)[|\nabla \phi| - 1] = 0. \tag{6}$$

The dummy variable τ represents a fictitious time that is used simply for this purpose. The sign function, $S(\phi)$ is defined as

$$S(\phi) = \frac{\phi}{\sqrt{\phi^2 + (\Delta x)^2}}, \tag{7}$$

where Δx is the grid spacing. This form ensures that $S(\phi)$ is well behaved near the interface where $\phi = 0$. For convenience of presentation, we take $\Delta x = \Delta y$, although this is not necessary. Following Fedkiw et al. [12], one can rewrite Eq. (6) in the form:

$$\frac{\partial \phi}{\partial \tau} + \left(\frac{S(\phi)\phi_x}{\sqrt{\phi_x^2 + \phi_y^2}} \right) \phi_x + \left(\frac{S(\phi)\phi_y}{\sqrt{\phi_x^2 + \phi_y^2}} \right) \phi_y = S(\phi). \tag{8}$$

We solve Eq. (8) using the same, fifth-order WENO algorithm in space and a third-order Runge–Kutta algorithm to discretize time, that is used to solve Eq. (5). This equation is evolved in τ until steady state, whereupon ϕ regains its property of being a signed distance function near the interface. For computational efficiency, we use the "localized" level set method, in which calculation of ϕ is performed only in a narrow region surrounding the interface.

Particles are included in the simulation by introducing additional distance functions that define the distance measured from the particle surface. We can then use a level set formulation identical to the one described above to advance the particle position. The acceleration of the particle is determined from the computed particle forces, described in the next section. The velocity at every time step can be computed from the acceleration of the particle. The advection of the distance function is trivial for undeformable particles because every point is moving at the same velocity. However, we maintain the description of the particle as a distance function in order to facilitate deformation for future work. The distance function is reinitialized after movement in the same manner described above.

Once the interface and particle distance functions are updated, calculation of the concentration field in the liquid and the solid can be performed. At this step, the interface is fixed, and we enforce thermodynamic equilibrium there using Eq. (4). The interface normal vector and curvature are computed from the distance function as

$$\mathbf{n} = \frac{\nabla \phi}{|\nabla \phi|}; \quad \kappa = \nabla \cdot \mathbf{n}. \tag{9}$$

We use a standard second-order finite difference scheme everywhere in the domain except at those nodes located at a distance of less than one grid spacing from the interface, where we use a modified stencil, with one side located on the interface and the other on the fixed grid point. A red-black Gauss–Seidel method is used to

solve the set of simultaneous equations for the concentration in each phase. This scheme enables the equations to be solved in parallel, as described elsewhere [54].

In order to calculate the drag force on the particle, we require the solution of the fluid flow field and the pressure field in the computational domain. We use the cell centered colocated finite difference flow solver developed by Marella et al. [32]. The method uses the distance functions to correct the finite difference stencils at the boundaries. It has been verified using a number of test cases, including droplet–wall interaction [30] and pure material solidification [56]. We give a brief description of the method here to provide the necessary background for understanding the results.

The governing equations for fluid flow with constant properties can be written as

$$\nabla \cdot \mathbf{v} = 0, \tag{10}$$

$$\frac{\partial \mathbf{v}}{\partial t} + \mathbf{v} \cdot \nabla \mathbf{v} = -\frac{1}{\rho}\nabla p + \frac{\mu}{\rho}\nabla^2 \mathbf{v}, \tag{11}$$

where ρ is the density, μ is the fluid viscosity, p is the pressure. These equations are solved using a two-level fractional step method. In the first step, an intermediate velocity vector $\mathbf{v}^\star$ is obtained from Eq. (11) by evaluating the inertial terms using an Adams–Bashforth scheme, the viscous terms using a Crank–Nicolson scheme, and omitting pressure:

$$\frac{1}{\Delta t}\left(\mathbf{v}^\star - \mathbf{v}^n\right) = -\frac{1}{2}\left(3\mathbf{v}^n \cdot \nabla \mathbf{v}^n - \mathbf{v}^{n-1} \cdot \nabla \mathbf{v}^{n-1}\right) + \frac{\mu}{2\rho}\left(\nabla^2 \mathbf{v}^\star + \nabla^2 \mathbf{v}^n\right). \tag{12}$$

The error in continuity in the velocity field $\mathbf{v}^\star$ is used to generate a pressure-Poisson equation:

$$\nabla^2 p = \frac{\rho}{\Delta t}\nabla \cdot \mathbf{v}^\star. \tag{13}$$

The final velocity is then obtained as a correction to $\mathbf{v}^\star$:

$$\mathbf{v}^{n+1} = \mathbf{v}^\star - \frac{\Delta t}{\rho}\nabla p. \tag{14}$$

The interface-modified finite difference scheme requires a velocity and a pressure boundary condition at the immersed interface. The velocities at the interface are defined by either Eq. (3) or by the velocity of the particle. By specifying Eq. (3) as the velocity boundary condition at the interface, we are assuming that no shrinkage occurs at the solidification front. A Neumann boundary condition for pressure, $\partial p/\partial n = 0$, is also applied at the interface. The method uses probing points and ghost nodes to enforce the pressure boundary conditions. (See Marella et al. for a detailed discussion [32].) A zero-shear stress condition is applied at the liquid far-field boundary to provide inflow of material into the system. Periodic boundary conditions are used for the boundaries parallel to the direction of the pulling velocity.

2.2. van der Waals and drag forces

After the concentration and velocity fields have been computed, the van der Waals repulsion forces and the pressure drag forces on the cells can be determined. The long range particle forces are computed based on the instantaneous pair-wise summation of dispersion forces, as proposed by Hamaker [18]. These are sometimes referred to as the non-retarded van der Waals forces. The pair-wise interaction potential between two bodies is computed as

$$E = -\int_{V_1} \mathrm{d}v_1 \int_{V_2} \mathrm{d}v_2 \frac{q^2 \lambda}{r^6}, \tag{15}$$

where V_1 and V_2 are the volumes of the two bodies, q is the number of atoms per unit volume, and r is the interaction distance. The London constant λ represents the energy associated with dispersion between two atoms. The interaction force is computed by differentiating the energy with respect to the interaction distance. Since we are interested in interactions of complex interfaces and particles, we integrate the force numerically. The method of numerical integration is illustrated in Fig. 4. Although Eq. (15) includes the summation of the

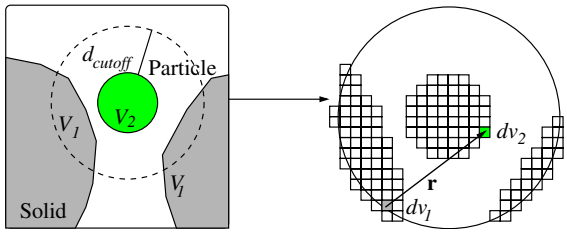

Fig. 4. The interface and the particle are discretized into volume elements. The interaction between all the volume elements in the particle with all the elements in the advancing interface are summed to produce an approximation for the van der Waals force on the particle.

dispersion energy between all of the atoms of the two interacting bodies, we limit the domains to a subset U for which r is less than a preset cutoff distance:

$$F_{\mathrm{vdW}} \approx 6q^2\lambda r^{-6} \sum_U \int_{V_1} \mathrm{d}v_1 \int_{V_2} \mathrm{d}v_2, \tag{16}$$

where the Hamaker constant is defined as $A \propto q^2\lambda$. It is clear from Eq. (16) that the interaction force is comprised of a geometric portion and a combination of material properties. We obtain the geometric portion by numerical integration, and use literature values for the material properties [43,53]. The advantage of this method is that it is applicable to arbitrary shapes and it can be applied to multiple particles interacting with multiple surfaces.

Catalina et al. [6] used the lubrication approximation to derive an analytical expression for the drag force on a cylinder close to a nearly flat interface, given by

$$F_{\mathrm{drag}} = 3\pi\sqrt{2}\frac{\mu V L}{\rho}\left(\frac{R}{d}\right)^{3/2}, \tag{17}$$

where R is the radius of the particle and L is the length of the cylinder. This form is valid only for the simple geometry they considered, and does not apply to the complex shapes that we encounter in this work. The accuracy of various expressions for the drag force on a particle has been studied by Garvin and Udaykumar [13]. From their work, it is clear that the formulation of the dynamic particle drag force is important when attempting to accurately simulate particle pushing.

A more general expression for the drag force that does not rely on restrictive shape approximations is needed to examine interactions between particles and complex interface morphologies. The pressure drag force can be computed directly from the pressure field surrounding the particle as

$$F_{\mathrm{drag}} = \int_S p \cdot \mathbf{n}\,\mathrm{d}S, \tag{18}$$

where S represents the surface area of the cell and $\mathbf{n}$ is the unit vector normal to the surface of the cell. No cellular deformation was observed during the cryomicroscopy experiments of particle/interface interaction. Therefore, we assume that the cell acts as a undeformable cylinder and Eq. (18) can be used to compute the force on the particle. Once the distance between the particle and the interface falls below $2\Delta x$, the fluid flow in the gap region is stopped and the region is considered a solid boundary.

Additional forces acting on the cell were also considered. The buoyancy force computed by Stefanescu et al. [46,49] is small in this case because the intracellular and extracellular environments are composed almost entirely of water. For the same reason, the material properties of the cell are assumed to be equivalent to those used for the freezing media. Therefore, the temperature field remains unchanged even with the addition of the cell into the computational domain.

2.3. Cell volume change

Cells respond to the changing concentration of their local environment by expressing water in order to reach osmotic equilibrium [19]. Supercooling of the water in the cell occurs when the cell does not remove

water fast enough to match the changing environment, and this has been shown to lead to intracellular ice formation [10,33,37]. High electrolyte concentrations also cause cell damage during cryopreservation [34,36,39,52]. The rate that the semi-permeable cell membrane is able to transport water was modeled by Mazur as [33]:

$$\frac{dv_{cell}}{dt} = k_{mb}A_{cell}(\pi_i - \pi_e), \tag{19}$$

where v_{cell} is the cell volume, t is time, k_{mb} is the permeability constant of the cell, A_{cell} is the surface area of the cell, and π_i and π_e are the intracellular and extracellular osmotic pressures, respectively. The osmotic pressure is related to the concentration by

$$\pi = MRT, \tag{20}$$

where M is the solution molarity, R is the universal gas constant and T is the temperature. We use Eq. (19) to determine the cell volume at any given time based on the average external concentration. We will use this information to determine the effects of various types of cell/interface interactions on cell volume change, which can further alter the response of the cell to the advancing solidification front.

To simulate the volume change over time, we determine that the time scale for volume change is much smaller than the time scale associated with the movement of the cell through the concentration field in front of the interface. This allows us to decouple the volume change from the motion of the particle at any given time step. We also assume that surface area of the cell is constant over a time step, and we neglect the temperature and concentration dependence of the membrane permeability. Combining Eqs. (19) and (20) using a fully explicit discretization gives

$$\frac{v_{cell}^{n+1} - v_{cell}^{n}}{\Delta t} = k_{mb}A_{cell}^{n}RT^{n}\left(M_i^n - M_e^n\right), \tag{21}$$

where n represents the value at the current time step and $n+1$ indicates the value at the next time step. The external concentration is determined by averaging the concentration at the nodes closest to the cell and T is the temperature computed from the thermal gradient, G, at the center of the cell.

2.4. Implementation details

The computation of the fluid flow field and diffusion ahead of the interface requires a fairly large computational domain, while the accurate calculation of the particle forces requires a relatively fine mesh. We address these conflicting requirements by using an adaptive mesh refinement scheme (AMR) [3,42,44,47,51] to resolve the intricate details of particle/interface interaction in a sufficiently large domain to include the diffusion lengths found in experiments.

The AMR is based on the introduction of pseudo-elements into the data storage scheme, allowing tracking of the refinement level in a region. The scheme, illustrated in Fig. 5, begins with a uniform coarse mesh. Each refined element is divided equally into four new elements, introducing five new nodes into the computational domain. The field value at each new edge node is computed by averaging those of the two closest original corner nodes, and the center node value is set to the average of the four corner nodes of the original element. The maximum refinement level, ℓ_{max}, is defined by the user. To ensure smooth transitions between refinement levels, an element can be refined only if its nearest neighbors have an equal or higher level of refinement. The refinement criterion is based on the magnitude of the distance function.

This scheme generates "hanging" nodes (missing a single nearest neighbor) at the transition between refinement levels. Linear interpolation between the closest edge nodes is used to calculate the concentration, velocity and pressure at these special nodes. The maximum refinement level will appear near the interface, where the gradients are largest, and a simulation parameter controls the mesh density sufficiently to resolve the various fields. Unrefinement of the mesh occurs after the interface moves far enough past an element that the increased accuracy provided by additional nodes is no longer needed.

The refinement/unrefinement process is implemented on a quad tree structure [44,47], so that parent and child elements are tracked, allowing the reconstruction of the original elements by fusion of the children.

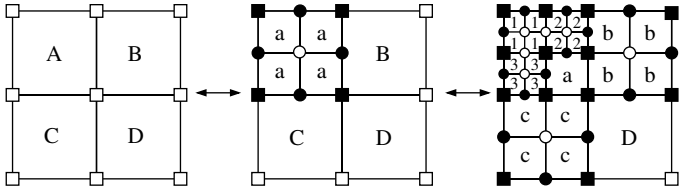

Fig. 5. An illustration of two refinement levels. The circles indicate new nodes created during the adaption phase. The black circles represent hanging nodes created by the adaption of the element. The squares are nodes that existed before the refinement of a given level. The black squares must be updated to account for the addition of the new nodes.

Unrefinement is done by fusion of sets of elements with the same parent element, all of whose distance functions are larger than a specified tolerance. The nearest neighbor elements must also be at the same refinement level as the child elements for unrefinement to take place. This ensures that there is a difference in refinement level of no more than one between any pair of neighboring elements.

In the level set method, it is quite natural to use different material properties in each domain. No special asymptotic analysis is necessary, even when the diffusivities are very different in the two domains. Different properties can also be specified for the particles that are interacting with the interface. The robust nature of the level set method allows us to examine a variety of problems that would be difficult to simulate using other methods.

3. Verification

This section summarizes several test cases that have analytical solutions to verify the code. The solidification modeling aspect of the code was tested by measuring the dispersion relation for the Mullins–Sekerka instability. The van der Waals force computation was tested by computing the repulsion force for two spheres at fixed distance, and the drag force computed in the code was compared to the analytical solution for a cylinder pushed ahead of a flat interface at fixed distance.

3.1. Interface stability

It is well known that in directional solidification of a binary alloy, a flat interface becomes morphologically unstable under some conditions. The two parameters which characterize the instability are called the morphological number, M, and a surface tension parameter S, given by

$$M = \frac{m_\ell C_0 (1 - k_0) V}{G_T D_\ell k_0}; \quad S = \frac{\Gamma V k_0}{D_\ell m_\ell C_0 (1 - k_0)}. \tag{22}$$

The marginal stability curve depends on wave number n [9]:

$$\frac{1}{M} = 1 - Sn^2 + \frac{2k_0}{1 - 2k_0 - \sqrt{1 + 4n^2}}. \tag{23}$$

A series of simulations was performed using the material properties listed in Table 1, starting with initial perturbations of various wavenumber. The temperature gradient was systematically varied to search for the marginal stability point. The results obtained after integrating for as many as 4000 time steps are shown in Fig. 6, compared to the analytical solution in Eq. (23). Acceptable agreement is found between the computed and analytical results. Some error appears at higher frequencies due to insufficient grid resolution. Note that the simulations were performed on larger domains for smaller values of n, to ensure that the results were not contaminated by the boundary conditions.

3.2. Two spherical particles

An analytical expression for the interaction force between two spherical particles, each of radius R, and whose centers are separated by a distance $d + 2R$ was developed by Hamaker [18]:

Table 1
Material and process parameters for simulations of marginal stability

Parameter	Value	Units
Γ	0.5	μm K
k_0	0.2	–
D_ℓ	1	$\mu m^2/s$
m_ℓ	−4	K/wt.%
C_0	0.1	wt.%
V	0.05	μm/s
Δx	0.125	μm
Δt	0.03125	s
S	0.015	–

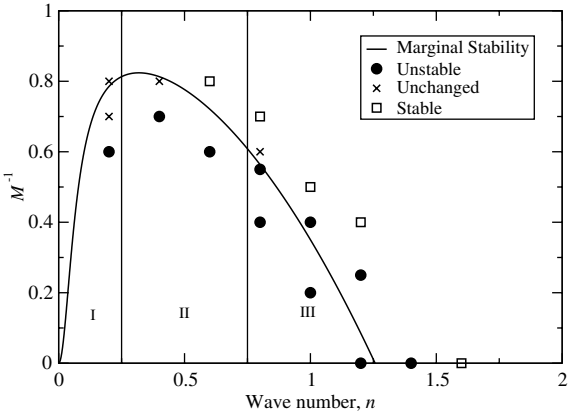

Fig. 6. Marginal stability analysis. The green "unchanged" squares represent simulations that did not produce a noticeable change after 4000 time steps. Stage I: 100 μm × 100 μm domain. Stage II: 75 μm × 75 μm domain. Stage III: 50 μm × 50 μm domain.

$$E_{\text{sphere}} = \frac{A}{6}\left(\frac{2R^2}{d(4R+d)} + \frac{2R^2}{(2R+d)^2} + \ln\left[\frac{d(4R+d)}{(2R+d)}\right]\right). \tag{24}$$

To test the code, we set $R = 1$ μm and $A = 10^{-19}$ J, and then computed the van der Waals force for $d = 0.1$ μm and $d = 2$ μm. The interaction energies computed using Eq. (24) corresponding to these two cases are 9.85×10^{-20} J and 1.32×10^{-22} J, respectively.

The spheres were enmeshed with a regular 3D grid, and the interaction was computed numerically using Eq. (16). The results of this verification problem are tabulated in Table 2.

3.3. Drag force on cylinder close to an interface

To check the drag force calculation, a cylinder of radius $R = 1$ was placed at a distance $d = 0.35$ from one boundary of a square domain, as illustrated in Fig. 7. The velocity on all of the boundaries of the domain was fixed, such that $u = 1$ and $v = 0$. The cylinder velocity was set to zero. We start with $p = 0$ inside the domain, and then integrate in time until steady state is reached. Uniform grid spacings of $\Delta x = 0.1$ and $\Delta x = 0.05$ were

Table 2
Comparison of analytical and numerical calculations of the interaction force between two spheres

d	Cutoff	Grid	E_{num} ($\times 10^{-24}$ J)	$E_{\text{Eq. (24)}}$ ($\times 10^{-24}$ J)	Error (%)
2.0	4.0	$26 \times 26 \times 26$	131.25	132.82	1.2
2.0	4.0	$41 \times 41 \times 41$	131.75	132.82	0.8
0.1	4.0	$61 \times 61 \times 61$	9.11×10^4	9.85×10^4	7.5

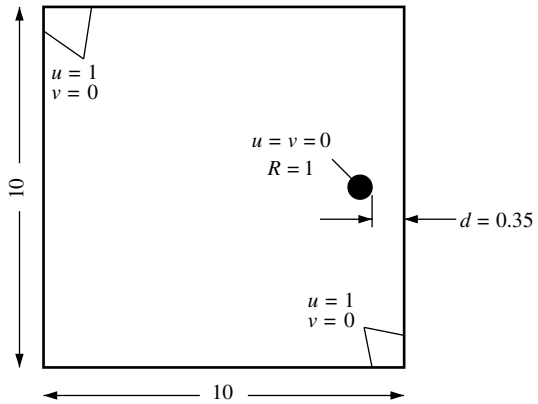

Fig. 7. Illustration of the computational domain and the boundary conditions associated with the calculation of the drag force on a cylinder close to a flat interface.

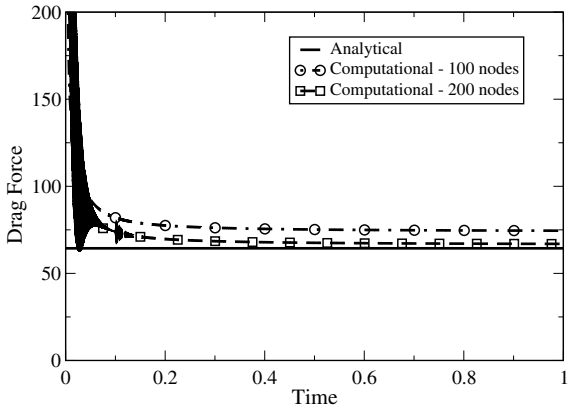

Fig. 8. Comparison of the analytical and computational solutions for the drag force on a cylinder close to a flat interface.

used to discretize the domain, and the fluid density and viscosity were set to 1. This problem configuration can be used to compute the drag force on a particle that is moving at a constant velocity ahead of a flat interface moving at the same velocity. This can be compared to the pressure drag force determined analytically from Eq. (17).

The results of the numerical simulations are illustrated in Fig. 8, along with the analytical solution computed from Eq. (17). Notice that small errors in the initial pressure cause some oscillations in the drag force, which disappear after an initial transient. The error in the computed drag force for the case using $\Delta x = 0.05$ is 3.6%.

4. Simulation results

In actual cryopreservation protocols, cells are dehydrated to about 20–30% of their original cell volume, the exact target depends on the particular type of cell. The reduction of water content in the cell helps to decrease the probability of harmful intracellular ice formation. The variance in post-thaw viability for a typical cryopreservation protocol can 30% or more. The results of this investigation suggest that one potential source of this variation involves differences in cell interaction with the ice interface, which can lead to significant differences in cell water content. In this section, we use the numerical methods described earlier to examine the effects of various types of interactions on cell volume change. Greater understanding and control of the

Table 3
Solidification parameters

Symbol	Meaning	Units	Values
V	Pulling velocity	μm/s	−0.05
G	Thermal gradient	K/μm	0.12
k_0	Segregation coefficient		0.2
m_ℓ	Slope of liquidus	K/wt.%	−4
C_0	Initial concentration	wt.%	0.1
D_ℓ	Diffusion coefficient (liquid)	$\mu m^2/s$	1
D_s	Diffusion coefficient (solid)	$\mu m^2/s$	1×10^{-4}
g_{cell}	Mass of cell	kg	1×10^{-12}
Γ	Surface energy	μm K	0.05
v	Kinematic viscosity	$\mu m^2/s$	1×10^7

interaction between cells and ice may lead to more uniform water content in each cell thus increasing survival rates during cryopreservation.

For the results shown below, many of the parameters are the same from one simulation to another. In the base case, a particle was placed 76.3 μm in front of an interface with an initial perturbation, $x = 2\cos 0.12\pi y$, in a domain of size 200 μm × 200 μm. The initial radius of the particle was 7.5 μm, the internal concentration within the cell was 0.020 M, and the cell membrane permeability constant was set to 1.5×10^4 $\mu m^3/N\,s$, which is the accepted value for the lymphoblastoid cells used in the cryomicroscopy experiments [22]. The Hamaker constant was set to $0.5 g_{cell}$ $\mu m/s^2$ where g_{cell} represents the average mass of a cell. A maximum refinement level of $l_{max} = 3$ was used for these simulations, corresponding to a minimum grid spacing and time step of $\Delta x = 0.5$ μm and $\Delta t = 0.25$ s, respectively. The forces on the cell are determined using computations that occur close to the gap region between the solidification front and the cell. Therefore, the highest grid refinement levels are used to discretize this region. The other solidification parameters used in the simulation are given in Table 3, and others changed for a particular case are highlighted below.

4.1. Flat interface

Several researchers have attempted to find the critical velocity that marks the boundary between pushing and engulfment of a cell by an ice interface [4,28,29,48]. However, it is important to note that this phenomenon is strongly affected by the cell volume change that occurs continuously during interaction. This could be responsible for the significant variations in reported values [29]. In this section, we use our simulations to examine the role of various parameters that can alter the dehydration characteristics of the cell, and show that indeed they have a significant effect on the interactions that occur between the cell and the interface.

Results of one such simulation are shown in Fig. 9. The contours represent the concentration field near the interface, and the black lines are streamlines generated from the relative motion of the fluid to the pulling velocity. The cell experiences significant loss of volume due to its extended exposure to the high concentration region close to the solidification front. Researchers have shown that decreasing the Hamaker constant [53] and increasing the solution viscosity promote engulfment [40], and we have found the same in our simulations. Further, the amount of cell volume change can also be affected by changes to k_{mb} and the initial internal concentration of the cell, as shown in the next simulation.

Fig. 10 illustrates the effect of changing the permeability constant, k_{mb}, of the cell from 1.5×10^4 to 1.5×10^3 $\mu m^3/N\,s$, maintaining the other parameters from the previous simulation. The lower permeability of the cell membrane results in a larger radius when it encounters the interface, and the cell is now engulfed by the interface because of the increased size. The cell experiences only a 40% volume loss, compared to 80% in the previous case, by limiting the amount of time that the cell is exposed to the high electrolyte concentrations close to the interface. Note that, in our simulations, the cell is assumed to stop expressing water once it becomes engulfed by the advancing ice interface, which explains the discontinuity

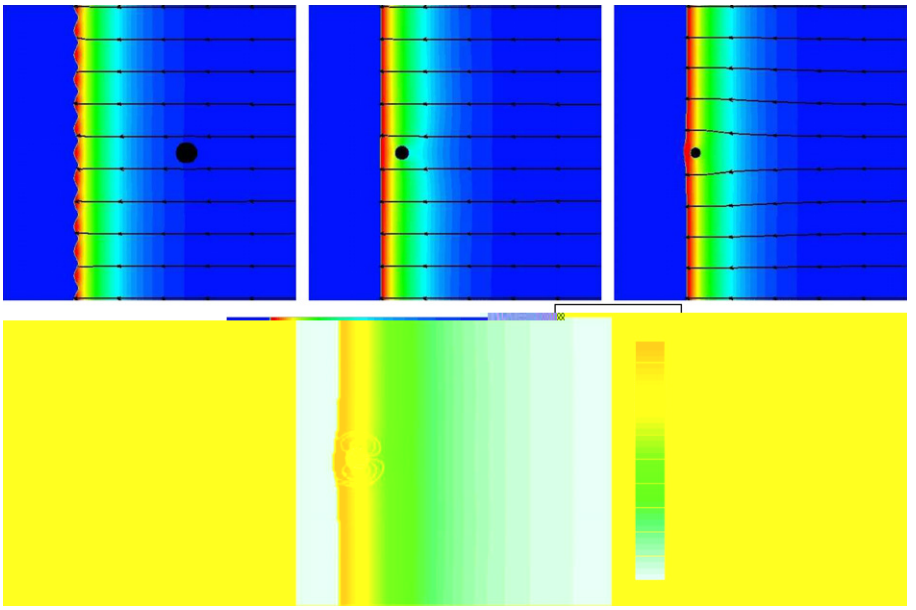

Fig. 9. Selected concentration and streamline contours, showing the interaction of a cell with a flat interface. Volume changes caused by the expression of water from the cell lead to it being pushed ahead of the interface. The streamlines in the top three panels are computed in the fixed laboratory frame, and in the lower panel in the reference frame translating with the pulling speed V_i.

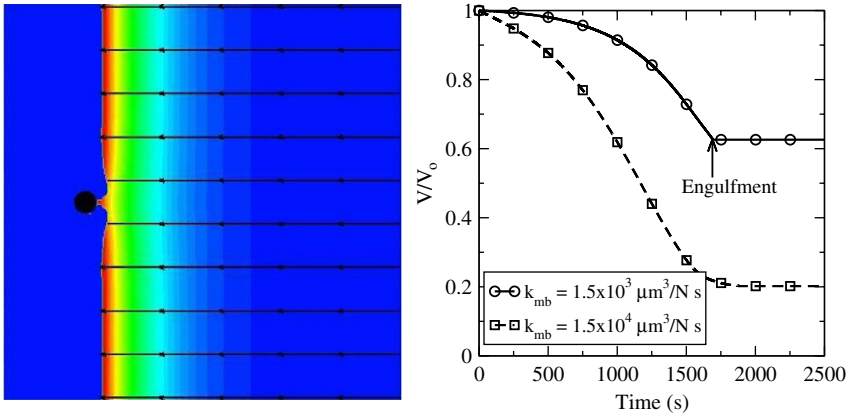

Fig. 10. Concentration field and volume change for cell with $k_{mb} = 1.5 \times 10^3$ μm^3/N s. The arrow indicates the approximate time that the cell is engulfed by the interface.

in volume change over time after engulfment has occurred. In practice, the cell may continue to dehydrate after engulfment, but experiments have shown that the rate of water loss is significantly slower under these conditions [21].

Preloading of the cell with high molecular weight additives [1] also encourages engulfment by increasing the initial internal concentration. To highlight this effect, we apply the same parameters as those use to simulate Fig. 9, except the initial internal cell concentration, C_{ic}, is changed from 0.02 M to 0.025 M to simulate the increased internal concentration due to preloading. The results of the simulation are shown in Fig. 11. The cell initially increases in volume in order to equilibrate its higher internal concentration with the external concentration in the extracellular liquid. This leads to a larger cell radius at the time of interface interaction, which in turn, increases the probability of cell engulfment. For this simulation, the cell is captured after 70% volume loss before engulfment prevents further volume change.

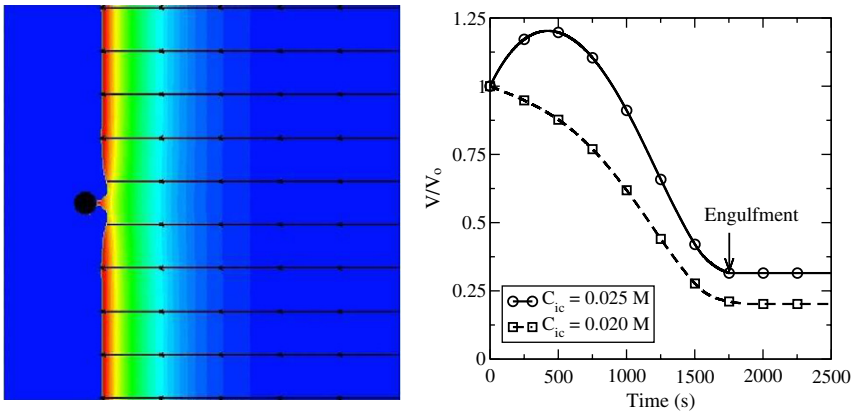

Fig. 11. Concentration field and volume change for cell with internal concentration of 0.025 M. The arrow indicates the approximate time that the cell is engulfed by the interface.

These results show that, in addition to the previously known importance of the Hamaker constant and the viscosity, chemical changes that affect cell volume change can have a dramatic effect on cell interaction with the solidifying interface. In the next section, we extend these studies to consider interfaces with more complex morphologies.

4.2. Interaction with complex interfaces

Cryopreservation protocols most commonly specify conditions that favor the development of dendritic interfaces. However, the complex interface structure make it more difficult to control the local environment surrounding the cell. We use our simulations to examine the effects of various types of cell/interface interactions on the exposure of the cell to high solute concentration, and discuss interactions that could be used to better control the local environment of the cell during cryopreservation. We also show qualitative agreement between simulation and the cryomicroscopy experiments described in Section 1. Although the experiments shown in Section 1 involved a large number of cells and cell clusters, we have restrict ourselves to examining the interactions between a single cell and the ice interface, because the physics involved with particle/particle interaction is beyond the scope of the present work.

The base case for these simulations is similar to the one for the flat interface, with the following exceptions: a maximum level of refinement $l_{\max} = 4$ was specified, corresponding to a minimum grid spacing of $\Delta x = 0.5$ μm and a time step size of $\Delta t = 0.25$ s. The maximum refinement level occurs close to the interfaces, which guarantees that the gap region between the particle and the interface will contain elements with the maximum level of refinement. The particle was held stationary for 300 s to allow the morphology of the interface to develop, and the thermal gradient was decreased to $G = 0.01$ K/μm to encourage the development of a dendritic interface. Deviations from the base case are noted below.

4.2.1. Entrapment by a dendritic interface

Cell entrapment is an important mechanism of cell/interface interaction in cryopreservation. Entrapment can occur at Hamaker constants that are much higher than those associated with flat interface particle pushing because the cells need to be displaced only slightly to align them with interdendritic spaces. For these simulations, we use a particle of radius 5.5 μm and a Hamaker constant of $50.0 g_{\text{cell}}$ μm/s^2. We examine the effects of cell location relative to interfacial features in order to show the ability of our computational method to study qualitatively the cell/interface behavior observed in cryomicroscopy.

Fig. 12 shows results from two different simulations intended to examine the difference in interaction when a particle is initially aligned with an interdendritic space, and when a particle is aligned with a tip. Cell dehydration is neglected for this case. The initial interactions are similar to those found in the

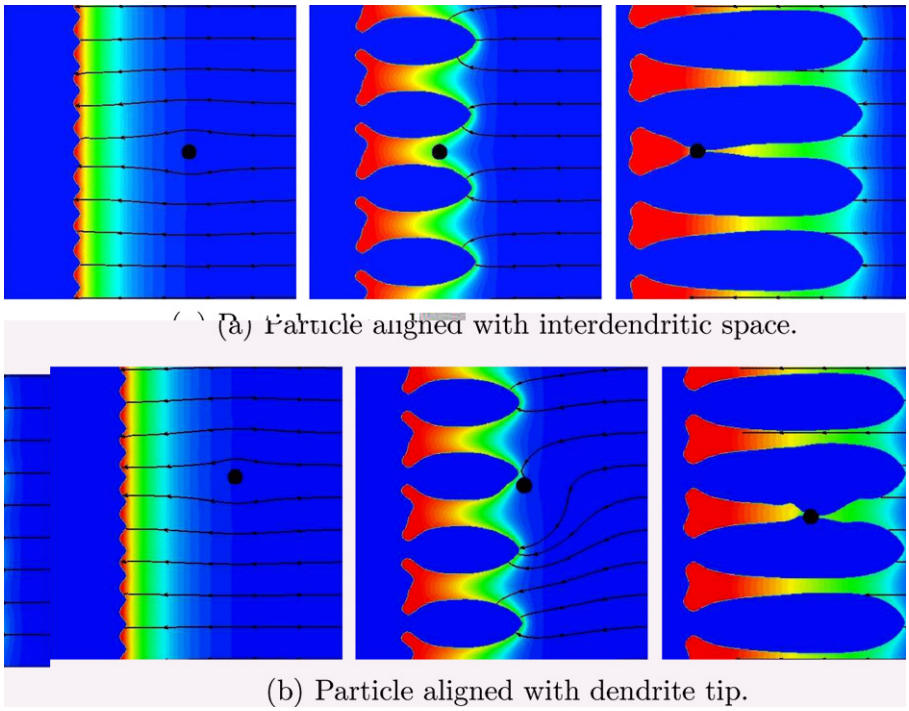

Fig. 12. The initial location of the particle can change the capture time of the particle. However, the particle in both cases becomes entrapped in the interdendritic space and is then captured.

cryomicroscopy experiments shown in Fig. 2. The particle aligned with the interdendritic space falls into the high concentration region where it is eventually captured by the interface. The particle aligned with the tip is pushed into an adjacent interdendritic space where it is also captured by the interface. Both of these particles are exposed for a significant length of time to high concentration regions before they are eventually encapsulated by the solid.

When volume change is also included in the simulation, the particle becomes small enough to position itself within an unsolidified, high concentration region close to the interface, as shown in Fig. 13. The exposure of the cell to this high concentration region leads to severe dehydration and potential damage to the cell. In this case, the cell loses almost 80% of its volume in an attempt to equilibrate the internal and external concentrations. These results show that although initial cell location can be used to modify the capture time, but the cell is still exposed to high concentrations regions for a significant amount of time regardless. In practice, cell entrapment is not an ideal cell capture mechanism because it exposes the cell to high concentrations of electrolytes for long periods of time, and the amount of volume change depends on the concentration in the interdendritic region, which is not easily controlled.

4.2.2. Pushing at a dendritic interface

Pushing by a flat interface also increases the amount of time that the cell interacts with high electrolyte concentrations. Pushing by a dendritic interface is more difficult to achieve because the particle has a tendency to become entrapped in the interdendritic spaces instead. However, stable pushing is possible with a dendritic interface, and in this section we show that this can actually lead to reduced exposure to high concentration regions located in the interdendritic spaces. Cell pushing also allows for greater control over the amount of dehydration that the cell experiences during cryopreservation protocols.

In this simulation, the initial interface perturbation is obtained by combining several cosine waves with random amplitudes as the initial condition. This leads to a morphology where the interdendritic spacing is small relative to the cell diameter, as shown in Fig. 14.

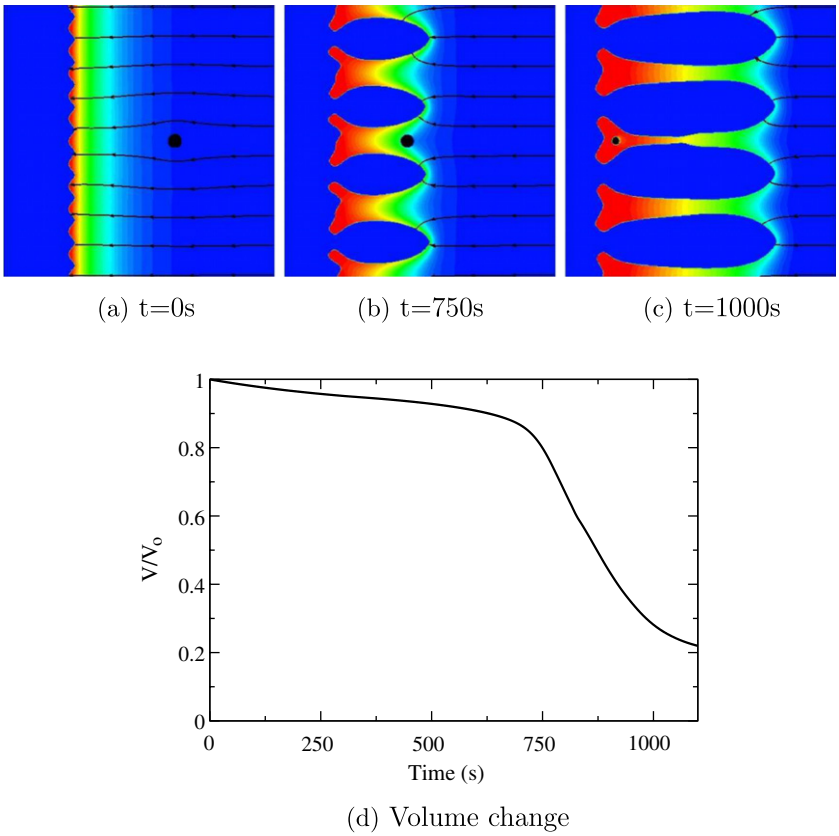

Fig. 13. Intermediate concentration field and change of cell volume over time for a particle that is pushed into an interdendritic space.

In this case, pushing can be stabilized by the interaction between the particle and multiple tips. This leads to significantly less exposure to the high concentration regions near the interface. Cell pushing could be used to control the water content in the cell, and then, the pulling velocity could be altered to encourage engulfment of the cell. In this way, cell volume could be manipulated to an extent that is difficult to achieve during cell entrapment.

4.2.3. Engulfment by a dendritic interface

Engulfment is the preferred method of cell capture during cryopreservation because it protects the cell from exposure to high electrolyte concentrations in the interdendritic spaces [20,24]. An example of cell engulfment during a cryomicroscopy experiment is shown in Fig. 15. To simulate this case, we use a cell with a radius of 7.5 μm and a Hamaker constant of $10.0g_{\text{cell}}$ μm/s^2. By reducing the Hamaker constant from the previous simulation, we are able to encourage engulfment of the cell by the dendritic front.

Fig. 16 illustrates the results. As the cell approaches, the dendrite tip begins to blunt because the cell acts as a diffusion barrier that concentrates solute in the gap between the two surfaces, and thereby slows the evolution of the ice front. The asymmetric interaction between the cell and the ice interface is similar to interaction experienced by cell (A) in Fig. 15. The asymmetric growth leads to a single dominant tip that eventually develops into the steady state morphology. Notice that the cell experiences limited interaction with the concentration field ahead of the dendrite tip and very little dehydration occurs. This is also potentially damaging behavior because intracellular ice formation is more likely in cells with large amounts of unbound water. However, the cell is protected from exposure to high electrolyte concentrations during this type of cell/interface interaction. Some combination of cell pushing and cell engulfment could be used to control the dehydration of the cell before engulfment by the dendritic tips.

(a) t=0s (b) t=600s (c) t=800s

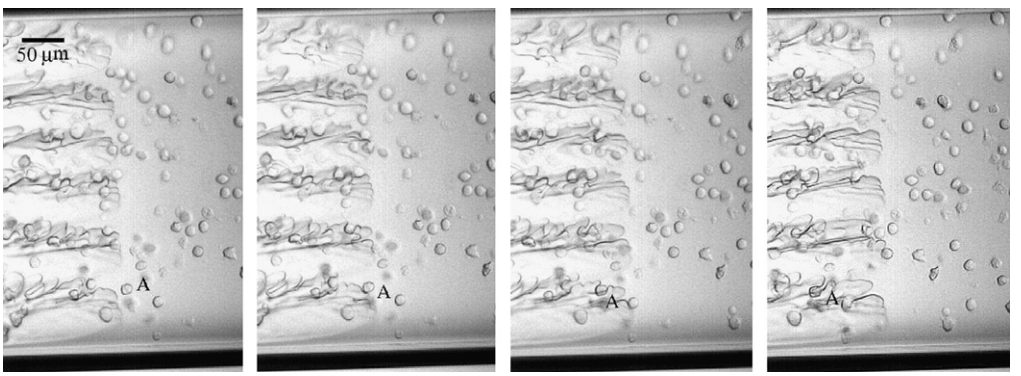

Fig. 15. Pulling velocity of 15 µm/s. Particle engulfment (A) by a solidify ice interface.

5. Conclusion

Simulating the interaction between cells and solidification interfaces with complex morphologies requires methods that can accurately determine the evolution of ice over time, the force between the interacting surfaces, and the response of the cell to its external environment. A level set method was used to evolve the interface structure over time, and an adaptive mesh refinement scheme was implemented to resolve the various length scales in the problem. Special methods were developed to determine the repulsive van der Waals forces between multiple surfaces with arbitrary geometries. Drag forces were computed using a fluid flow field computed from a two step fractional step method that does not rely on analytical solutions of the lubrication approximation. Cell response to its local environment was also introduced into the simulations, allowing us to examine the role of cell volume change due to dehydration on the interaction between the cell and the advancing solidification front. These methods have allowed us to simulate different types of interactions between complex interface morphologies and cells.

The volume change of the cell during interaction with a solidification front is important in determining the type of interaction that occurs between the two surfaces. Dehydration of the cell can be controlled by altering the membrane permeability constant of the cell, or by increasing the initial internal concentration of macromolecules in the cell. The ability to control the response of the cell to its external environment can be used to encourage engulfment of the cell, which has been shown to protect the cell from exposure to high electrolyte concentrations and severe dehydration.

We have also shown that different types of cell interaction with the ice interface can lead significant differences in the final volume of individual cells. Cell entrapment tends to expose the cell to high concentrations of electrolytes in the interdendritic regions, where the final solidification conditions are difficult to control. Cell pushing can be used to control the dehydration of the cell more easily, and it avoids exposing the cell to high concentrations that develop in the interdendritic spaces. Cell engulfment protects the cell from high concentration regions but it leaves the cell vulnerable to intracellular ice formation. However, a combination of cell pushing and cell engulfment can be used to control the dehydration of the cell and provide limited interaction with high electrolyte concentrations.

We have focused our attention on the interactions between single particles and an advancing ice interface. Cell/cell interactions become more important for suspensions that contain higher volume fractions of cells, which is more typical of cryopreservation conditions. The interaction of clusters of cells with ice could be simulated by assuming that the clusters act like a single particle with a radius that represents the overall size of the cell cluster. Increasing the radius of the representative particle would increase the probability of engulfment and pushing by the interface. On the other hand, the intermolecular forces between cells and the fluid flow around various arrays of single cells and cell clusters can lead to complex dynamic behavior that is not yet included in our model. In the future, it would be interesting to include these phenomena in our simulations in order to study their effects on the partitioning of cells by the ice interface.

References

[1] J.P. Acker, in: J.G. Baust (Ed.), Advances in Biopreservation, CRC Press Inc., Florida, 2006, p. 298.
[2] B.P. Athreya, J.A. Dantzig, S. Liu, R. Trivedi, On the role of confinement on solidification in pure materials and binary alloys, Philos. Mag. 86 (24) (2006) 3739–3756.
[3] R.J. Braun, B.T. Murray, Adaptive phase-field computations of dendritic crystal growth, J. Cryst. Growth 174 (1997) 41.
[4] V.L. Bronstein, Y.A. Itkin, G. Ishkov, Rejection and capture of cells by ice crystals on freezing, J. Cryst. Growth 52 (1981) 345–349.
[5] M. Carin, M. Jaeger, Numerical simulation of the interaction of biological cells with an ice front during freezing, Eur. Phys. J. Appl. Phys. 16 (2001) 231–238.
[6] A.V. Catalina, S. Mukherjee, D.M. Stefanescu, A dynamic model for the interaction between a solid particle and an advancing solid/liquid interface, Metall. Mater. Trans. A 31A (2000) 2559–2568.
[7] S. Chen, B. Merrimann, S. Osher, P. Smereka, A simple level set method for solving Stefan problems, J. Comput. Phys. 135 (1) (1997) 8–29.
[8] P.B. Conrad, D.P. Miller, P.R. Cielenski, J.J. de Pablo, Stabilization and preservation of Lactobacillus acidophilus in saccharide matrices, Cryobiology 41 (1) (2000) 17–24.
[9] S.H. Davis, Theory of Solidification, Cambridge University Press, New York, 2001.
[10] K.R. Diller, J. Sosa, P.G. Martinez-Pastrano, Intracellular ice formation in glycerolized red cells, Cryobiology 12 (1975) 580.

[11] B. Echebarria, R. Folch, A. Karma, M. Plapp, Quantitative phase-field model of alloy solidification, Phys. Rev. E 70 (2004) 061604.
[12] R.P. Fedkiw, T. Aslam, B. Merriman, S. Osher, A non-oscillatory Eulerian approach to interfaces in multimaterial flows (the ghost fluid method), J. Comput. Phys. 152 (1999) 457–492.
[13] J.W. Garvin, H.S. Udaykumar, Particle-solidification front dynamics using a fully coupled approach Part II: comparison of drag expressions, J. Cryst. Growth 252 (2003) 467–479.
[14] J.W. Garvin, H.S. Udaykumar, Effect of a premelted film on the dynamics of particle-solidification front interactions, J. Cryst. Growth 290 (2005) 602–614.
[15] F. Gibou, R. Fedkiw, R. Caflisch, S. Osher, A level set approach for the numerical simulation of dendritic growth, J. Sci. Comp. 19 (1–3) (2003) 183–199.
[16] B. Grossmann, K. Elder, M. Grant, M. Kosterlitz, Directional solidification in two and three dimensions, Phys. Rev. Lett. 71 (20) (1993) 3323–3326.
[17] L. Hadji, Morphological instability induced by the interaction of a particle with a solid–liquid interface, Eur. Phys. J. B 37 (1) (2004) 85–89.
[18] H.C. Hamaker, The London-van der Waals attraction between two spherical particles, Physica 10 (1947) 1058–1071.
[19] H.R. Harmison, K.R. Diller, J.R. Walsh, C.M. Neils, J.J. Brand, Measurement of cell volume loss in the liquid region preceding an advancing phase change interface, Ann. N.Y. Acad. Sci. 858 (1) (1998) 276–283.
[20] A. Hubel, E.G. Cravalho, B. Nunner, C. Körber, Survival of directionally solidified B-lymphoblasts under various crystal growth conditions, Cryobiology 28 (1992) 183.
[21] A. Hubel, T.B. Darr, private communications.
[22] A. Hubel, T.B. Darr, J.A. Norman, Freezing characteristics of genetically modified lymphocytes for the treatment of MPS, Cell Trans. (1999) 521–530.
[23] H. Ishiguro, B. Rubinsky, Mechanical interactions between ice crystals and red blood cells during directional solidification, Cryobiology 31 (1994) 483–500.
[24] H. Ishiguro, B. Rubinsky, Mechanical interactions between ice crystals and red blood cells during directional solidification, Cryobiology 31 (1994) 483.
[25] J.-H. Jeong, N. Goldenfeld, J.A. Dantzig, Phase field model for three-dimensional dendritic growth with fluid flow, Phys. Rev. E 64 (2001) 041602.
[26] A. Karma, W.-J. Rappel, Quantitative phase-field modeling of dendritic growth in two and three dimensions, Phys. Rev. E 57 (4) (1998) 4323–4349.
[27] Y.-T. Kim, N. Goldenfeld, J.A. Dantzig, Computation of dendritic microstructures using a level set method, Phys. Rev. E 62 (2) (2000) 2471–2474.
[28] C. Köber, Phenomena at the advancing ice–liquid interface: solutes, particles, and biological cells, Rev. Biophys. 21 (1989) 229–298.
[29] G. Lipp, S. Galow, C. Köber, G. Rau, Encapsulation of human erythrocytes by growing ice crystals, Cryobiology 31 (1994) 305–312.
[30] H. Liu, S. Krishnan, S. Marella, H.S. Udaykumar, Sharp interface Cartesian grid method II: a technique for simulating droplet interactions with surfaces of arbitrary shape, J. Comput. Phys. 210 (2005) 32–54.
[31] L. Mao, H.S. Udaykumar, J.O.M. Karlsson, Simulation of micro-scale interactions between ice and biological cells, Int. J. Heat Mass Transfer 46 (2003) 523.
[32] S. Marella, S. Krishnan, H. Liu, H.S. Udaykumar, Sharp interface Cartesian grid method I: an easily implemented technique for 3D moving boundary computations, J. Comput. Phys. 210 (2005) 1–31.
[33] P. Mazur, Kinetics of water loss from cells at subzero temperatures and the likelihood of intracellular freezing, J. Gen. Physiol. 47 (1963) 347–369.
[34] P. Mazur, Limits to life at low temperatures and at reduced water contents and water activities, Origins Life Evol. Biospheres 10 (2) (1980) 137–159.
[35] P. Mazur, K.W. Cole, Influence of cell concentration on the contribution of unfrozen fraction and salt concentration to the survival of slowly frozen human erythrocytes, Cryobiology 22 (1985) 509.
[36] P. Mazur, K.W. Cole, Roles of unfrozen fraction, salt concentration and changes in cell volume in the survival of frozen human erythrocytes, Cryobiology 26 (1989) 1.
[37] P. Mazur, R.H. Miller, Survival of supercooled yeast, Cryobiology 3 (1967) 365.
[38] P. Mazur, W.F. Rall, N. Rigopoulos, Relative contributions of the fraction of unfrozen water and of salt concentration to the survival of slowly frozen human erythrocytes, Biophys. J. 36 (1981) 653–675.
[39] P. Mazur, N. Rigopoulos, Contributions of unfrozen fraction and of salt concentration to the survival of slowly frozen human erythrocytes: influence of warming rate, Cryobiology 20 (1983) 274.
[40] G.J. Morris, M. Goodrich, E. Acton, F. Fonseca, The high viscosity encountered during freezing in glycerol solutions: effects on cryopreservation, Cryobiology 52 (3) (2006) 323–334.
[41] B. Nestler, A.A. Wheeler, L. Ratke, C. Stöcker, Phase-field model for solidification of a monoeutectic alloy with convection, Physica D 141 (2000) 133–154.
[42] N. Palle, J.A. Dantzig, An adaptive mesh refinement scheme for solidification problems, Metall. Trans. A 27A (1996) 707.
[43] J. Pötschke, V. Rogge, On the behaviour of foreign particles at an advancing solid–liquid interface, J. Cryst. Growth 94 (1989) 726–738.
[44] N. Provatas, N. Goldenfeld, J. Dantzig, Efficient computation of dendritic microstructures using adaptive mesh refinement, Phys. Rev. Lett. 80 (1998) 3308.

[45] N. Provatas, Q. Wang, M. Haataja, M. Grant, Seaweed to dendrite transition in directional solidification, Phys. Rev. Lett. 91 (15) (2003) 155502.
[46] D. Shangguan, S. Ahuja, D.M. Stefanescu, An analytical model for the interaction between an insoluble particle and an advancing solid/liquid interface, Metall. Mater. Trans. A 23A (1992) 669–680.
[47] M.S. Shephard, P.L. Baehmann, K.R. Grice, The versatility of automatic mesh generators based on tree structures and advanced geometric constraints, Commun. Appl. Numer. Methods 4 (1988) 379.
[48] J.K. Spelt, D.R. Absolom, W. Zingg, C.J. van Oss, A.W. Neumann, Determination of the surface tension of biological cells using the freezing front technique, Cell Biophys. 4 (1982) 117–131.
[49] D. Stefanescu, A. Moitra, A. Kacar, B. Dhindaw, The influence of buoyant forces and volume fraction of particles on the particle pushing/entrapment transition during directional solidification of Al/SiC and Al/Graphite composites, Metall. Mater. Trans. A 21A (1990) 231–239.
[50] A.K. Sum, R. Faller, J.J. de Pablo, Molecular simulation study of phospholipid bilayers and insights of the interactions with dissacharides, Biophys. J. 85 (2003) 3636–3645.
[51] M. Sussman, A.S. Almgren, J.B. Bell, P. Colella, L.H. Howell, M.L. Welcome, An adaptive level set approach for incompressible two-phase flows, J. Comput. Phys. 148 (1999) 81–124.
[52] L.E. Towill, P. Mazur, Osmotic shrinkage as a factor in freezing injury in plant tissue cultures, Plant Phys. 57 (1976) 290–296.
[53] C.J. Van Oss, R.F. Giese, J. Norris, Interaction between advancing ice fronts and erythrocytes: mechanism of erythrocyte destruction upon freezing and influence of cryoprotective agents, Cell Biophys. 18 (1991) 253–261.
[54] K. Wang, A. Chang, L.V. Kale, J.A. Dantzig, Parallelization of a level set method for simulating dendritic growth, J. Parallel Distrib. Comput. 66 (2006) 1379–1386.
[55] W.F. Wolkers, F. Tablin, J.H. Crowe, From anhydrobiosis to freeze-drying of eukaryotic cells, Comp. Biochem. Physiol. A: Mol. Integr. Physiol. 131 (3) (2002) 535–543.
[56] Y. Yang, H.S. Udaykumar, Sharp interface Cartesian grid method III: solidification of pure materials and binary solutions, J. Comput. Phys. 210 (2005) 55–74.